

# Dynamics of Seaweed-Inspired Piezoelectric Plates for Energy Harvesting from Oscillatory Cross Flow

\*

## Abstract

Inspired by the vibrations of aquatic plants such as seaweed in the unsteady flow fields generated by free-surface waves, we investigate a novel device based on piezoelectric plates to harvest energy from oscillatory cross flows. Towards this end, numerical studies are conducted using a flow-structure-electric interaction model to understand the underlying physical mechanisms involved in the dynamics and energy harvesting performance of one or a pair of piezoelectric plates in an oscillatory cross flow. In a single-plate configuration, both periodic and irregular responses have been observed depending on parameters such as normalized plate stiffness and Keulegan-Carpenter number. Large power harvesting is achieved with the excitation of natural modes. Besides, when the time scale of the motion and the intrinsic time scale of the circuit are close to each other the power extraction is enhanced. In a two-plate configuration with tandem formation, the hydrodynamic interaction between the two plates can induce irregularity in the response. In terms of energy harvesting, two counteracting mechanisms have been identified, shielding and energy recovery. The shielding effect reduces plate motion and energy harvesting, whereas with the energy recovery effect one plate is able to recover energy from the wake of

---

\*

another for performance enhancement. The competition between these mechanisms leads to constructive or destructive interactions between the two plates. These results suggest that for better performance the system should be excited at its natural period, which should be close to the intrinsic time scale of the circuit. Moreover, using a pair of plates in a tandem formation can further improve the energy harvesting capacity when conditions for constructive interaction are satisfied.

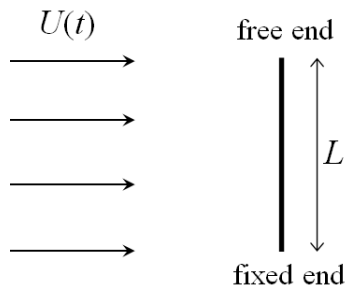
## **1 Introduction**



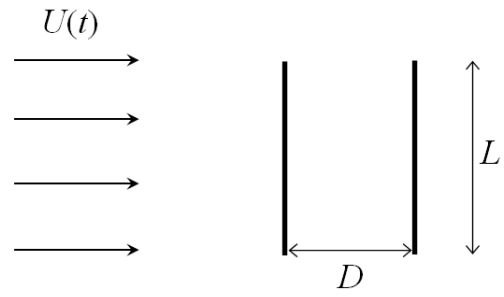




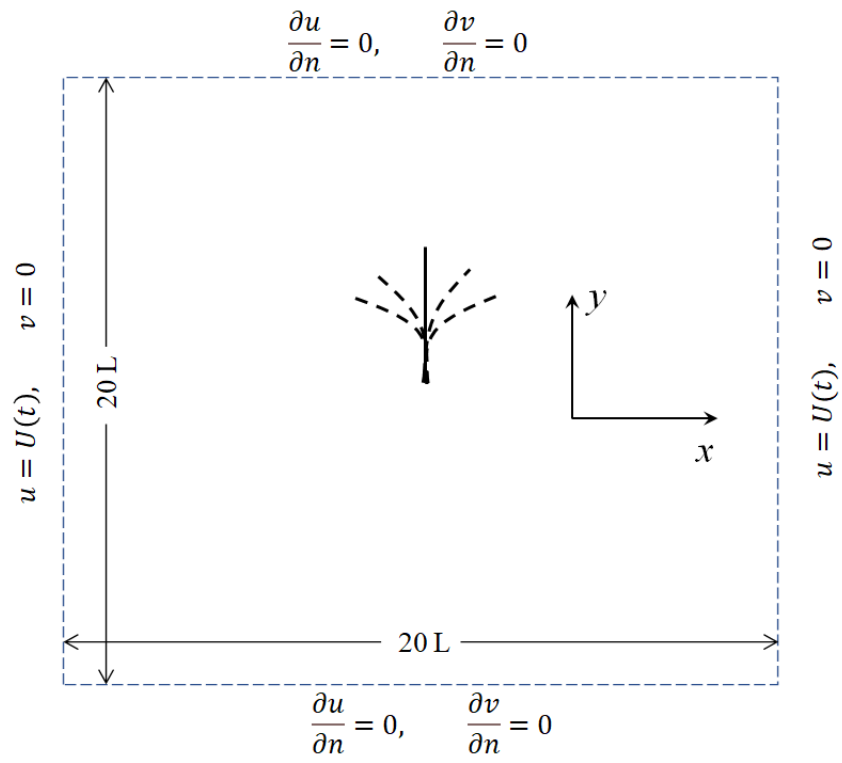
## 2 Problem description



(a)



(b)





### 3 Materials and methods

#### 3.1 Governing equations

$$\left( \frac{\mathbf{u}}{\rho} + \mathbf{u} \cdot \nabla \mathbf{u} \right) - \nabla \cdot \boldsymbol{\tau} = \mathbf{f} \quad \mathbf{x}$$

$$\nabla \cdot \mathbf{u} = 0$$

$\mathbf{x} \equiv$

$\mathbf{u} \equiv$

$\mathbf{f}$

$$\frac{\mathbf{X}}{\rho} - \nabla \cdot \boldsymbol{\tau} = \mathbf{f} \quad \mathbf{x}$$

$\mathbf{X}$

$\boldsymbol{\tau} = \mathcal{A} \nabla \mathbf{n}$

$\mathcal{A}$

$\mathbf{F}$

$\mathbf{X} \cdot \mathbf{X}$

$$\frac{\nu}{\mathcal{A}} = \nu - \mathcal{A} \left( \frac{\mathbf{X}}{\sqrt{\nu}} \cdot \mathbf{n} \right)$$

§

$$-\int \nu$$

$$-\sqrt{\nu}$$

$$\frac{\mathbf{X}}{\sqrt{\nu}} = \tau - \left( \frac{\mathbf{X}}{\sqrt{\nu}} \right) - \left( \sqrt{\nu} \frac{\nu}{\mathbf{n}} \right) - \mathbf{F}$$

$$\frac{\nu}{\mathcal{A}} = \nu - \sqrt{\nu} \left( \frac{\mathbf{X}}{\sqrt{\nu}} \cdot \mathbf{n} \right)$$

$$\mathcal{A} \sqrt{\nu}$$

$$-\int \nu$$

$\mathbf{X} \quad \mathbf{F} \quad \nu$

(3) to (5).

### 3.2 Immersed-boundary formulation and numerical implementation

The coupled fluid-structure-electric equations in §3.1 are solved by using a model we have developed and validated in previous publications [19, 26] based on an immersed-boundary framework in the literature [25, 27]. Specifically, the force density on the fluid exerted by the structure  $\mathbf{f}$  and the force density on the structure exerted by the fluid  $\mathbf{F}$  are related through a Dirac Delta function so that

$$\mathbf{f}(\mathbf{x}) = \int_{\Gamma} \mathbf{F}(\mathbf{x}') (\mathbf{X}(\mathbf{x}') - \mathbf{x}) \quad (9)$$

where  $\Gamma$  represents the structure. Furthermore, to enforce the no-flux and no-slip conditions at the fluid-structure interface, the force  $\mathbf{F}$  is evaluated by using a penalty method [25, 26]

$$\mathbf{F}(\mathbf{x}) = \int_0^{\infty} [\mathbf{U}(\mathbf{x}) - \mathbf{V}(\mathbf{x})] e^{-\beta t} + [\mathbf{U}(\mathbf{x}) - \mathbf{V}(\mathbf{x})] e^{-\beta t} \quad (10)$$

where  $\mathbf{V}$  is the structural velocity and  $\mathbf{U}$  is the fluid velocity at the fluid-structure interface obtained as

$$\mathbf{U}(\mathbf{x}) = \int_{\Omega} \mathbf{u}(\mathbf{x}') (\mathbf{x} - \mathbf{X}(\mathbf{x}')) \mathbf{x} \quad (11)$$

where  $\Omega$  is the fluid domain.  $\beta$  and  $\gamma$  are numerical parameters with sufficiently large negative values.

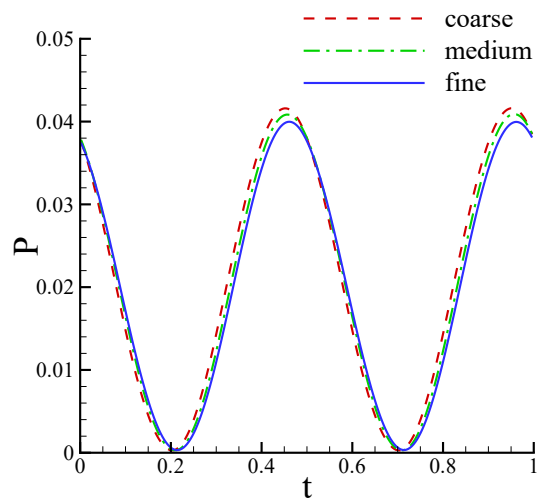
Thus formulated, the equations, including the fluid dynamics equations, the structural dynamics equation, and the circuit equation, are solved with a finite-difference

## 4 Results

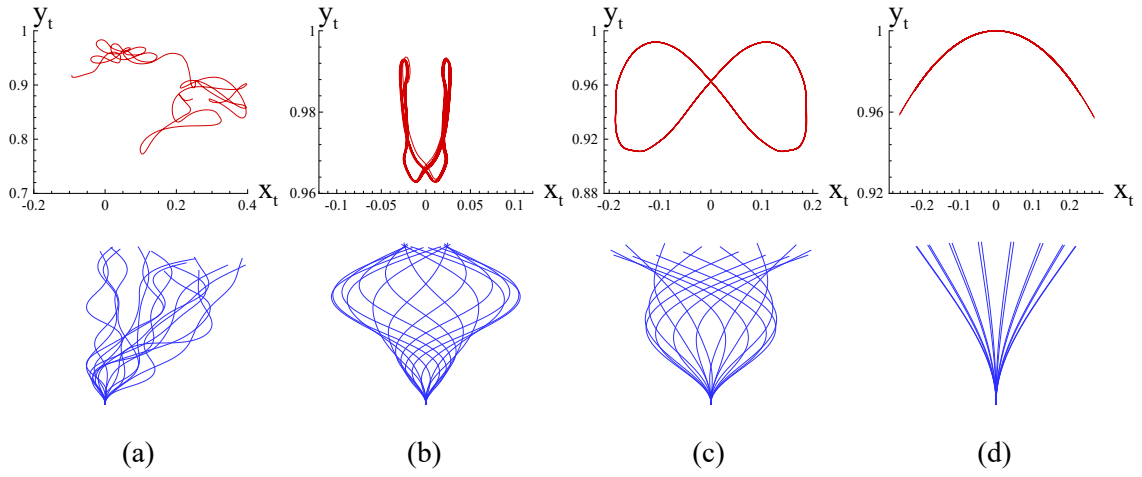
### 4.1 A single plate

- 
- 
- 

—



$$K_C \cdot \kappa \cdot t^{-4} \cdot P$$



$$\kappa \cdot \dots \quad \kappa \quad -3 \quad x_t, y_t \quad \kappa \cdot \dots$$

$$\kappa \quad \cdot \quad K_C \quad \cdot$$

— —

—

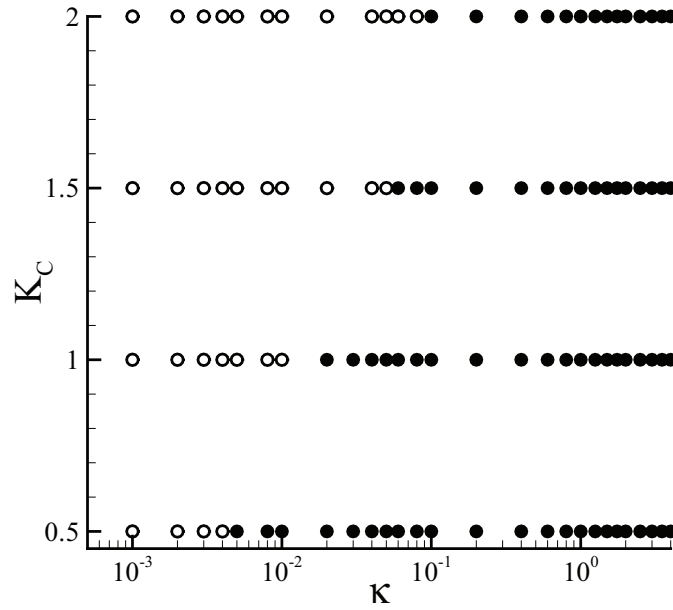


Figure 5: Occurrence of irregular ( $\circ$ ) and periodic ( $\bullet$ ) responses at various combinations of  $\kappa$  and  $K_C$ .

$\kappa$  is reduced. Further reduction of  $\kappa$  leads to irregular response so that no higher modes have been observed. For structural safety and reliable energy harvesting, the irregular response shall be avoided since it is unpredictable.

Figure 5 demonstrates a map of periodic versus irregular responses at different combinations of  $\kappa$  and  $K_C$ . It is seen that at a given  $K_C$ , the response becomes irregular when  $\kappa$  falls below a threshold value. This value increases when  $K_C$  is raised. For example, when  $K_C = 0.5$ , the transition to irregularity occurs at  $\kappa = 5 \times 10^{-3}$ . When  $K_C$  is raised to 1, the threshold value of  $\kappa$  becomes  $2 \times 10^{-2}$ . At the upper end of  $K_C$  considered in this study (i.e.,  $K_C = 2$ ), this value rises to 0.1.

In periodic responses, we characterize the motion and energy harvesting perfor-

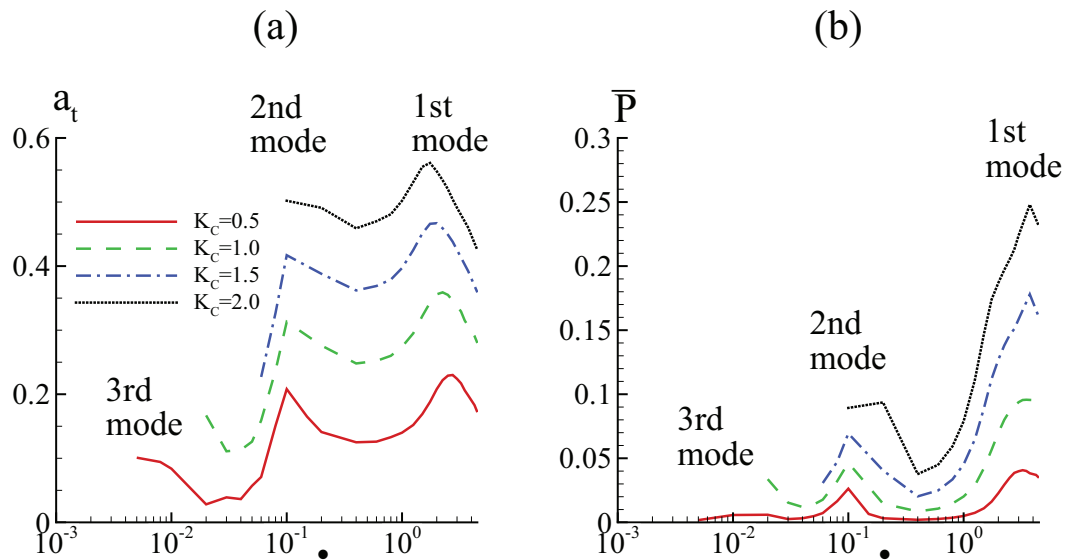


Figure 6: (a) Amplitude of the top end  $a_t$  and (b) time-averaged power extraction capacity  $\bar{P}$  as functions of  $\kappa$  at various values of  $K_C$ . The modes in this figure are illustrated in Fig. 4.

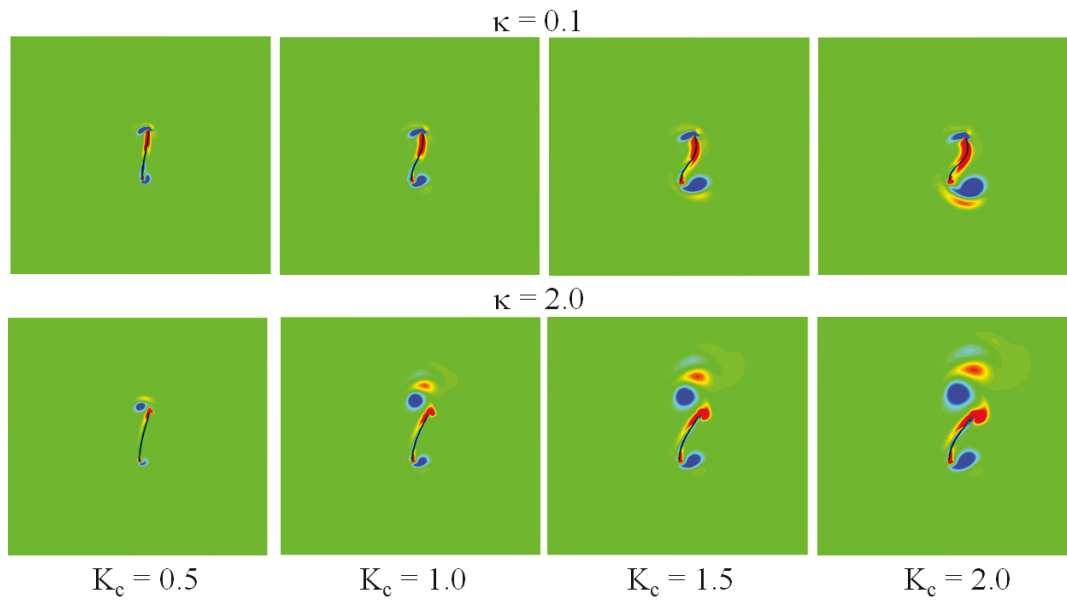


Figure 7: Flow fields visualized through vorticity contour ranging from -10 (blue) and 10 (red) at  $\kappa = 0.1$  and 2.0 with various values of  $K_C$  for a single plate.  $t = T/2$ .



—

—

—

—

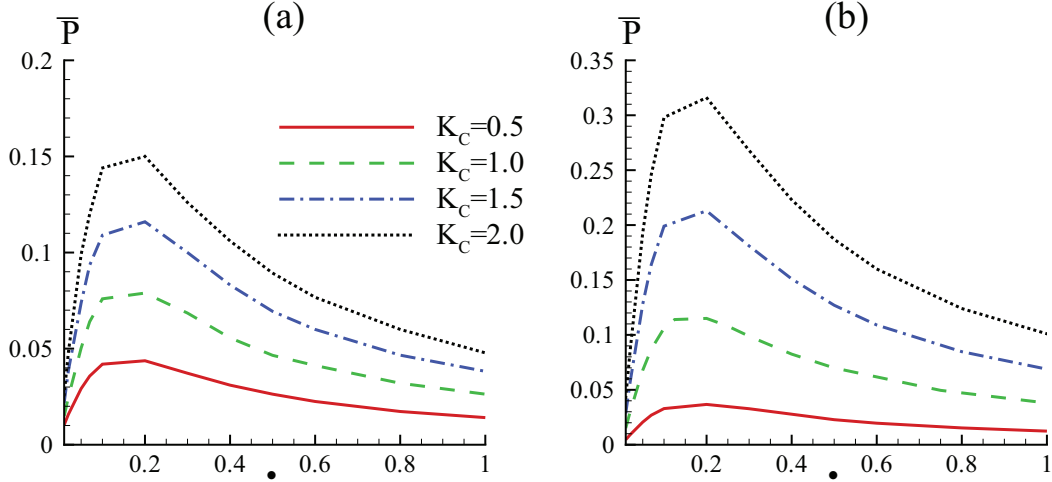


Figure 8: Time-averaged power extraction capacity  $\bar{P}$  as function of  $\beta$  at various values of  $K_C$  when (a)  $\kappa = 0.1$  and (b)  $\kappa = 2.0$ .

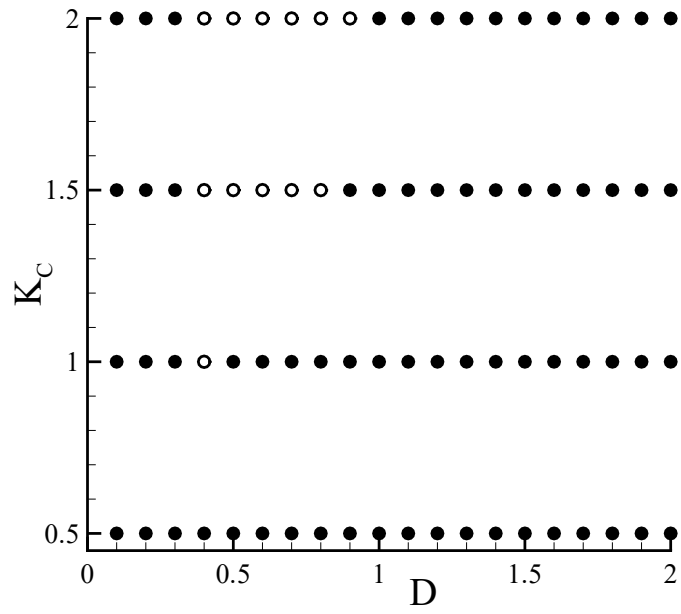
detailed vorticity distribution there exist considerable differences between the two plates. Most notably, with the stiff plate there are strong vortices shed from the top end. However, in the soft plate the vortex shedding from the top end is greatly mitigated. This is attributed to the diminished relative motion between the free end of the plate and the surrounding flow (i.e., the feathering effect) when the stiffness is low. This phenomenon will have interesting effects on the hydrodynamic interaction between two tandem plates, which will be discussed later.

To examine the effect of the electric parameters, we simulate the soft and stiff plates with  $\beta$  (which combines the resistance  $R$  and the capacitance  $C$ ) ranging from 0.01 to 1. According to the results (see Fig. 8), optimal power harvesting is achieved when  $\beta \sim 0.2$ . This is reminiscent of the finding that when the time scale of structural deformation matches the intrinsic time scale of the circuit, the power extraction is maximized [14, 16]. In the literature, this occurs when  $\beta\omega = O(1)$  ( $\omega$  is

## 4.2 Two tandem plates

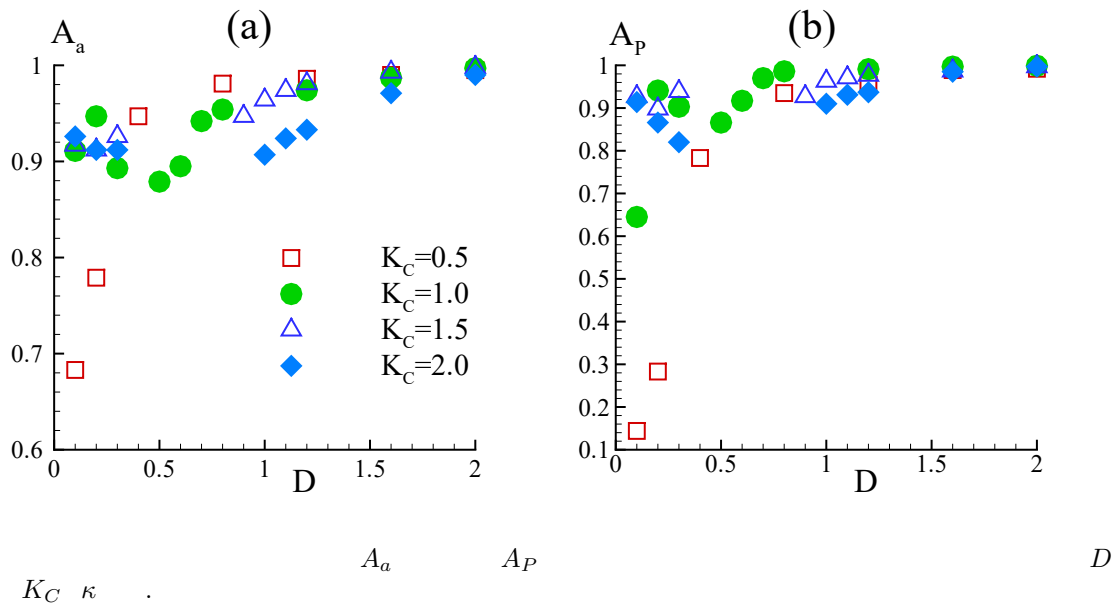
§

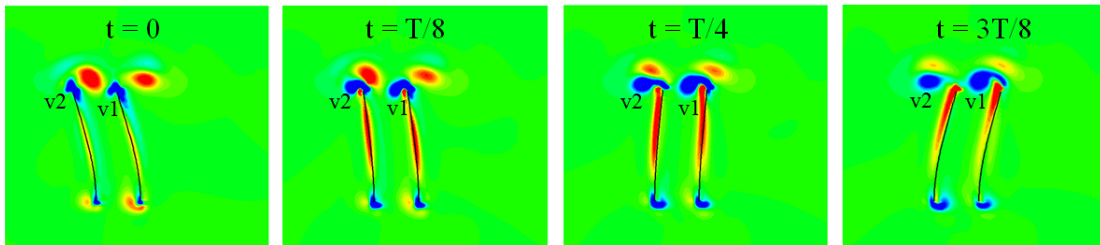
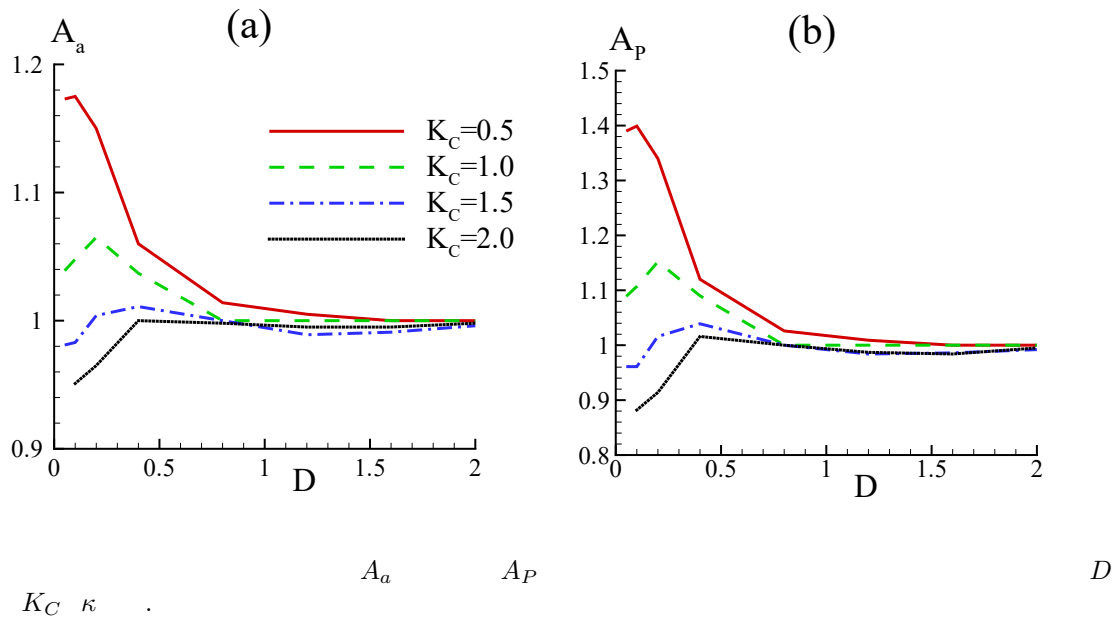
( $\bar{\quad}$   $\bar{\quad}$ ) ( $\bar{\quad}$ )  $\bar{\quad}$   $\bar{\quad}$



$D$   $K_C$   $\kappa$  . . .

—





$\kappa$  .  $K_C$  .  $D$  .



## 5 Conclusions



—

—

—



## Data Availability Statement

## References





